The interaction of pyrite {100} surfaces with O$_2$ and H$_2$O: Fundamental oxidation mechanisms

KEVIN M. ROSSO,[1,*] UDO BECKER,[2] AND MICHAEL F. HOCHELLA JR.[1]

[1]Department of Geological Sciences, Virginia Polytechnic Institute and State University, Blacksburg, Virginia 24061, U.S.A.
[2]Universität Münster, Institut für Mineralogie, Corrensstrasse 24, D-48149 Münster, Germany

ABSTRACT

The interaction of gaseous O$_2$, H$_2$O, and their mixtures with clean {100} surfaces of pyrite (FeS$_2$) were investigated in ultra-high vacuum using scanning tunneling microscopy and spectroscopy (STM-STS), ultraviolet photoelectron spectroscopy (UPS) and ab initio calculations. He I UPS spectra of O$_2$ exposed surfaces show that the density of states decreases at the top of the valence band but increases deeper in the valence band. These changes indicate oxidative consumption of low binding energy electrons occupying dangling bond surface states localized on surface Fe atoms, and the formation of Fe-O bonds. No such changes in the valence band spectra are observed for pyrite surfaces exposed to H$_2$O. However, UPS spectra of surfaces exposed to mixtures of O$_2$ and H$_2$O demonstrate that the combined gases more aggressively oxidize the surface compared to equivalent exposures of pure O$_2$. Atomically resolved STM images of O$_2$ and O$_2$-H$_2$O exposed surfaces show discrete oxidation "patches" where reacted surface Fe sites have lost surface state density to the sorbed species. STS spectra show the removal of highest occupied and lowest unoccupied surface state density associated with dangling bond states consistent with the interaction of sorbates with surface Fe sites. Ab initio cluster calculations of adsorption energies and the interaction of O$_2$ and water species with the surface show that O$_2$ dissociatively sorbs and H$_2$O molecularly sorbs to surface Fe. For the mixtures, the calculations indicate that H$_2$O dissociatively sorbs when O$_2$ is present on the surface. Charge population analyses also show that the surface S sites become more electropositive in this environment which should allow for easier formation of S-O surface bonds, thus promoting the production of sulfate during oxidation.

INTRODUCTION

The geochemical, environmental, and technological significance of pyrite oxidation has resulted in many studies devoted to understanding this oxidation process. Low temperature aqueous solution experiments (e.g., Goldhaber 1983; Wiersma and Rimstidt 1984; McKibben and Barnes 1986; Moses et al. 1987; Nicholson et al. 1988; Moses and Herman 1991; Williamson and Rimstidt 1994) collectively have unraveled the general principles of the overall reaction. One of the most notable characteristics of pyrite oxidation is that, in the end products, only S is oxidized, whereas Fe is divalent in both the crystal and as a dissolved species in solution. The stepwise oxidation of S from a –1 state in pyrite disulfide to a +6 state in sulfate involve very fast reactions and thus attempts to understand the sequential oxidation of sulfur have met with little success. Stable isotope tracer studies (Taylor et al. 1984; Reedy et al. 1991) showed that O$_2$ in the end product SO$_4^{2-}$ is dominantly derived from H$_2$O; both pH and temperature have minimal effects on this outcome. Hence, dissociated H$_2$O species play a key role as reactants in the overall oxidation process and any mecha-

nistic model must account for this.

Understanding the individual reaction mechanisms at the pyrite surface is based largely on surface analytical approaches. Studies of the oxidation of pyrite in air, have mostly relied on X-ray photoelectron spectroscopy (XPS) data (Buckley and Woods 1987; Mycroft et al. 1990; Karthe et al. 1993; Nesbitt and Muir 1994; Schaufuss et al. 1998). Various initial air oxidation products have been documented, including iron oxides and/or hydroxides and iron sulfate. Many questions remain regarding formation of these products at the surface.

These questions can be addressed at the atomic scale using local probe techniques such as scanning tunneling microscopy (STM). Studies at this scale (Eggleston 1994; Eggleston et al. 1996) are difficult to perform because of the generally rough surface produced by cleaving, but have given us a great deal of insight into site-specific oxidation reactions. STM observations of pyrite focussed on {100} surface formed by cleaving Fe-S bonds, which were oxidized in air, show the initial development of oxidation products across the {100} surface and the participation and nearest neighbor influence of iron states in oxidation (Eggleston et al. 1996). Pyrite also presents a similarly reactive irregular surface via cleaving when the fracture deviates from {100} and when S-S bonds are broken. Monosulfide states on this surface have been shown to be quickly quenched by exposure to air as documented using XPS (Schaufuss et al. 1998).

---

*Present address: Environmental Molecular Sciences Laboratory, Pacific Northwest National Laboratory, P.O. Box 999, K8-96, Richland, Washington 99352, U.S.A. E-mail: kevin.rosso@pnl.gov

This work focuses on the in-vacuum controlled oxidation of the {100} areas on the cleaved surface using scanning tunneling microscopy and spectroscopy (STM-STS) and ultraviolet photoelectron spectroscopy (UPS). This experimental setup allows for atomic scale examination of the surface before and after controlled exposures to O_2, H_2O and mixtures thereof. The goal is to examine the adsorption of these reactants on the surface and to determine their relative roles in the initial stages of oxidation. These observations are made in the context of previous work establishing the site-specific electronic structure of the {100} surface (Rosso et al. 1999).

METHODS

Principal instrumentation, samples, and gas dosing

STM-STS and UPS were performed in a OMICRON compact UHV lab operating at a base pressure of 1×10^{-10} mbar using samples and preparation methods as described in Rosso et al. (1999). The UHV system is equipped with an in-house built gas leak manifold for controlled gas bleeds to various parts of the main chamber. Pure H_2O vapor was prepared starting from de-ionized H_2O in a fused quartz thimble attached to the gas introduction manifold. The H_2O was purged of dissolved atmospheric gases by three cycles of freezing, pumping off the residual vapor, and then thawing. High purity O_2 (99.99%) was used. Mixtures of O_2-H_2O were prepared in the gas introduction manifold prior to dosing by filling a closed section with the equilibrium vapor pressure of H_2O at room temperature, and then introducing O_2 and adjusting the total pressure until the desired mole ratio was reached, based on ideal mixing. The total gas pressure was measured using a capacitance manometer. The gases were introduced to the main analytical chamber through a precision leak valve and the pressure was monitored using an ionization gauge. Typical dosing pressures were in the high 10^{-8} to the low 10^{-7} mbar range. The gas exposure was recorded in units of Langmuir (1 L = 1.33×10^{-6} mbar · s) by integrating the pressure vs. time curve.

Ultraviolet photoelectron spectroscopy

UPS spectra were collected using He I (21.2 eV) radiation and a pass energy of 10 eV. The sample surface was oriented normal to the lens axis of the analyzer. The sample stubs, the outer surface of the pyrite prism, and the notches in the prisms used in the UPS experiments were sputter coated with a visible layer of Au to isolate the Fe spectral data to that coming from the cleaved surface. Because UV radiation has been shown to alter pyrite surfaces to a non-conducting state (Rosso et al. 1999), spectra were collected on individual samples that had been previously exposed to the gas(es) of interest but not to UV light. Samples exposed to UV radiation were subsequently found to be unusable for surface reaction studies. The absolute binding energy scale of the UPS spectra was referenced to the sample Fermi level, which was determined in Rosso et al. (1999).

Scanning tunneling microscopy and spectroscopy

The UHV STM-STS methods were described in Rosso et al. (1999). Here, STS was performed on surfaces that had been incrementally dosed with O_2. Each of the spectra on O_2 ex-

posed surfaces represent the average of 125 curves collected over a period of 5 minutes in using a variation of CITS mode over a 1 nm² area on the surface, between O_2 exposures. STS spectra were collected independent of atomic scale images, precluding knowledge of whether the tip was located in either an oxidized or unoxidized area of the surface. This approach is based on the assumption that, over the course of 5 minutes, piezo-drift will cause the tip to be displaced over a random distribution of locations on the surface, providing area-averaged data. At each spectroscopy point, the tip raster was paused, the feedback loop was turned off, the voltage ramp was applied, the loop was re-engaged, and imaging resumed. The time required to collect each spectrum was 63 ms including 50 μs delays between each spectral datum to let capacitive transients die out.

Ab initio calculations

Ab initio calculations of adsorption reactions on pyrite clusters were performed using Gaussian94 (Frisch et al. 1995) on a 27-atom stoichiometric cluster previously used (Rosso et al. 1999). An electron core pseudopotential basis set known as SBKJC VDZ ECP was chosen for both Fe (Stevens et al. 1992) and S (Stevens et al. 1984). Several minor modifications were made for the Fe basis set. The most diffuse (exponent 0.04) sp function was removed to save unwarranted computational expense and the exponents of the most diffuse sp and d functions were energy optimized simultaneously. The optimal exponent for these gaussian functions was 0.161 which was similar to the original 0.1213 (sp) and 0.1382 (d) values. For O_2 and H, a standard LANL2DZ ECP basis set was used (Dunning and Hay 1976). The calculations were performed at the unrestricted (open shell) Hartree-Fock level of theory so that spins states of adsorbed molecules and surface atoms could be calculated. Adsorption energies were estimated by comparing total electronic energies of various optimized cluster-gas configurations. Geometry optimizations of the full cluster have demonstrated the stability of the structure and a resistance to significantly reconstruct, in agreement with the known surface structure (Pettenkofer et al. 1991; Rosso et al. 1999). Therefore, for purposes of reducing computational costs, geometry optimizations in this study were restricted to the position of the adsorbate molecule with respect to the fixed cluster coordinates.

RESULTS AND DISCUSSION

Ultraviolet photoelectron spectroscopy

He I UPS valence band spectra of cleaved pyrite exposed to O_2, H_2O, mixtures of O_2/H_2O, and air were collected to observe changes in the valence band (VB) structure of the surface. We first focus on O_2 exposed surfaces. Samples exposed to pure O_2 show a progressive oxidation and an apparent passivation toward oxidation by approximately 20 L exposure. The oxidation of the surface is generally manifested in the UPS spectra as a decrease in the density of filled states near the top of the valence band and a concomitant appearance of peaks deeper in the valence band (Fig. 1a). These features are more clearly revealed in difference spectra (Fig. 1b). In the negative intensity region of the difference spectra, the decrease in the DOS at the top of the VB is focused between 0–5 eV binding energy and
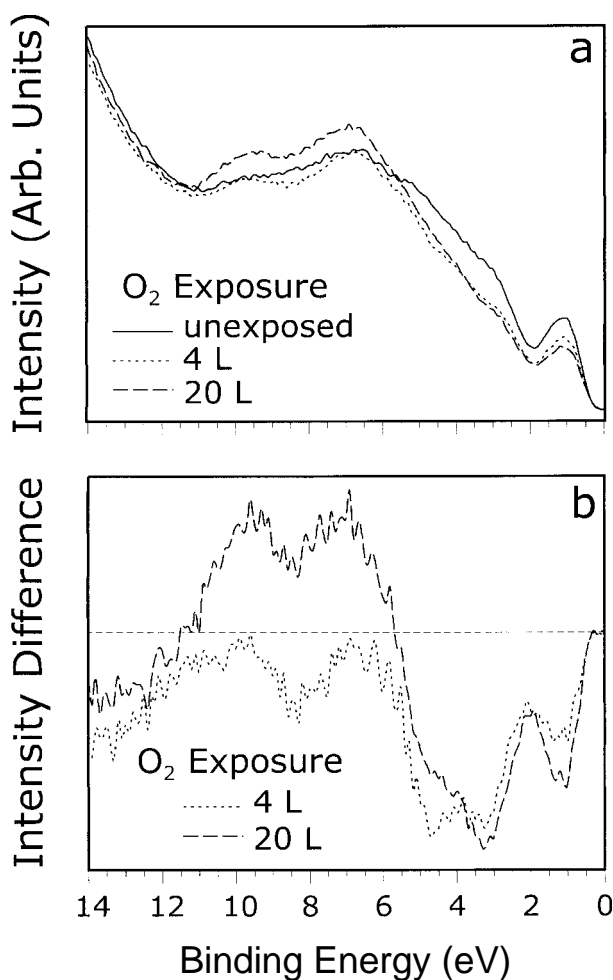
FIGURE 1. He I UPS valence band spectra (**a**), and difference spectra (**b**) for pristine pyrite surfaces and those exposed to O_2 gas. Difference spectra = reacted-pristine spectra.

this decrease is divided into two regions by a feature that can be described as a less negative "peak" centered at about 2 eV. Based on the electronic structure at the {100} surface (Rosso et al. 1999), and because sorbed O_2 species are not expected to contribute states between 0–5 eV (see below), it is possible to relate features in the difference spectra to states associated with the pyrite surface. The DOS decrease in the lowest binding energy region at about 1 eV can be attributed primarily to the oxidative quenching of partially filled surface states that have Fe $3d_{z^2}$ character and the depopulation of non-bonding Fe 3d states. Dangling bond surface states on Fe are predicted to be highest energy occupied states (Rosso et al. 1999). Incoming O_2 is expected to interact with these dangling bonds and form Fe-O bonds across the surface, although this point will be further developed below.

The difference peak at 2 eV (Fig. 1b) represents a loss of state density which is less sensitive to the presence of sorbed O species. Calculations of the surface electronic structure using band theory predict that S 3p orbitals contribute state density

over a wide range of binding energies with the highest energy S 3p states overlapping the Fe 3d non-bonding states at 1 eV (Rosso et al. 1999). States that lie just below the energy of the non-bonding Fe 3d states should be primarily derived from these S 3p orbitals. This is true for bulk and surface environments as it has been shown that surface S 3p states are not energetically shifted from their bulk band energies (Rosso et al. 1999). If it is assumed at this point that sorbed O species primarily depopulate Fe 3d states, then the peak shown in the UPS difference spectra at 2 eV binding energy represents surface S 3p states. The energy range below this, between about 3–5 eV, corresponds to Fe 3d–S 3p bonding states. Decreases in this region are attributed to the depopulation of Fe-S bonding states and weakening of lattice bonds at the surface.

The UPS difference spectra also show an increased DOS deeper in the valence band appearing as broad peaks at approximately 7 and 10 eV (Fig. 1b). Valence band DOS increases in this energy range are common for sorbed O containing species on sulfides and oxides (see Brundle 1974; Pettenkofer et al. 1991; Henrich and Cox 1994; Eggleston et al. 1996). These increases can be attributed to the development of new states due to the formation of Fe-O bonds across the surface. The two new photopeaks may be correlated with an Fe-O bonding state at 10 eV, and non-bonding O 2p states at 7 eV (see Pettenkofer et al. 1991). However, in this case, the UPS spectra do not provide unambiguous information regarding the specific sorbed species on the surface, i.e., O_2, O_2^-, O^-, or O^{2-}, and therefore we cannot properly address the issue of surface speciation using the spectra alone.

Surfaces exposed up to 10 L of pure H_2O gas showed no detectable change in the valence band structure. This was not surprising, as previous results showed that H_2O only sorbs to pyrite surfaces at low temperature and desorbs at room temperature (Guevremont et al. 1997; Pettenkofer et al. 1991). Water physisorbed molecularly to Fe sites at 100 K was reversibly desorbed upon heating to room temperature (Pettenkofer et al. 1991).

Valence band spectra of surfaces exposed to certain mixtures of O_2 and H_2O showed that the combination of the two gases most aggressively oxidized the surface. Similar changes in the valence band structure were observed for surfaces exposed to O_2-H_2O mixtures relative to pure O_2, but more than an order of magnitude less exposure was found to produce spectral features of the same intensity (Fig. 2). Surfaces oxidized by 0.1 L of 50 mol% O_2 mixtures showed an equivalent reduction in state density between 0–5 eV as that for 20 L of pure O_2. This mixture also resulted in a more rapid build-up of state density in the energy range of 5–11 eV. The degree of surface oxidation due to this exposure is roughly the same as that caused by a 30 second exposure to air (uncontrolled humidity) (Fig. 2). He I photoemission from 2p states of chemisorbed O have been documented as a broad feature at 6 eV for sorbed O on Si (111) (Wagner and Spicer 1974) and at 7 and 11 eV for molecular H_2O on TiO_2 (110) (Kurtz et al. 1989). Pettenkofer et al. (1991) documented valence band peaks at 7, 10, and 13 eV for physisorbed H_2O on pyrite {100}. Similar to the case for pure O_2 exposures, the close spacing between photopeaks derived from O 2p states in the binding energy range where we
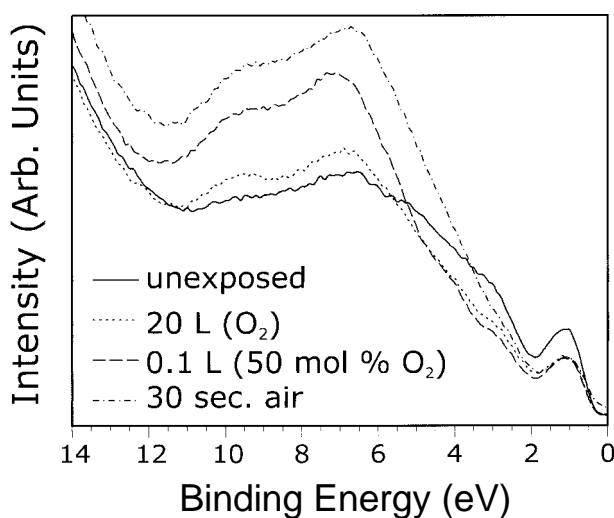
FIGURE 2. He I UPS valence band spectra comparing pristine pyrite surfaces with those exposed to O_2, O_2-H_2O, and air.

FIGURE 3. He I UPS valence band difference spectra of pyrite surfaces that were exposed to similar doses of different mixtures of O_2-H_2O, and a surface that was exposed to a much larger dose of pure O_2.

see DOS increases precludes the determination of the surface speciation of the adsorbate molecules. Because the distinction between the possible types of sorbed species is not explicit in the UPS data, this issue will be addressed further in a theoretical section below.

The 1 to 1 mole ratio of O_2-H_2O mixture turned out to be the most facile at effecting oxidative changes in the valence band spectra (Fig. 3). Similar difference features can be seen for oxidation by O_2 and by O_2-H_2O mixtures. As the concentration of O_2 in the mixture is reduced, the difference spectra approach that for pure H_2O, i.e., no change. On the other hand, the pure O_2 endmember results in oxidation of a much lesser degree (Fig. 3).

Irradiating the in-vacuum cleaved pyrite surface with several types of incident beams (low energy electron beams, Mg$K\alpha$ X-rays and especially He I UV), alters the electronic structure of the surface toward a non-conductive state (Rosso et al. 1999). Thus, it was of interest to examine the effect of this alteration on the surface reactivity. Samples were analyzed using He I UPS before and after exposure to various O_2 doses. Samples that were initially UV irradiated displayed no change in the upper valence band DOS when exposed up to 166 L O_2. The alteration of the surface to a non-conductive state is apparently accompanied by an inertness of the surface toward oxidation by O_2. The possibility that this could be related to photo-enhanced oxidation of the surface by background gases in the analytical chamber can be ruled out based on the good agreement between our He I UPS spectra of the unexposed in-vacuum cleaved surface and identical analyses performed elsewhere (Li et al. 1974; Van der Heide et al. 1980; Pettenkofer et al. 1991).

Scanning tunneling microscopy

STM is a very sensitive local probe of the electronic density of valence and conduction bands states near the Fermi level. Atomically resolved UHV STM images of pyrite {100} at low negative or positive bias display a face-centered cubic array of
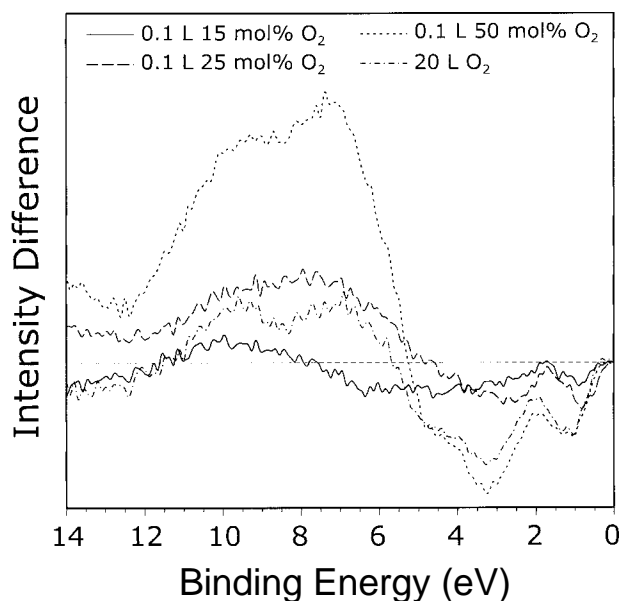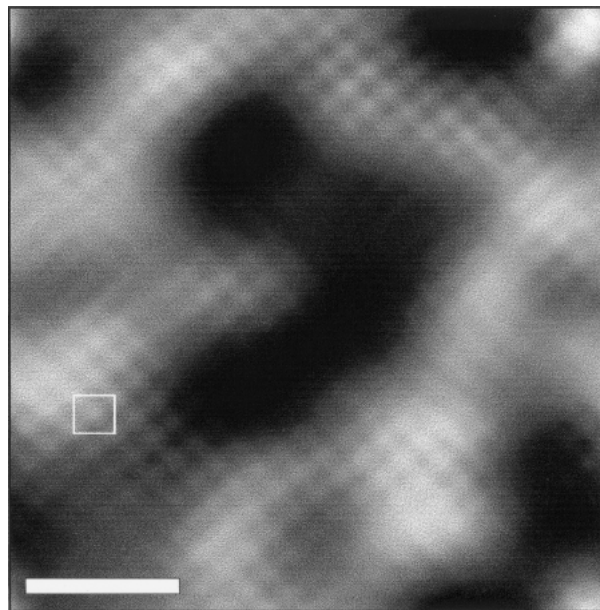

FIGURE 4. Atomic-scale topographic UHV STM image of an in-vacuum cleaved pyrite {100} surface after exposure to 4 L O_2. The tunneling conditions were –0.1 V bias and 3 nA setpoint current. The image was band pass FFT filtered to remove noise. The scale bar represents 20 Å. A unit cell is outlined. The image shows oxidation features in the form of dark "patches" where Fe sites have reacted with O_2.

high tunneling current sites (bright sites) at Fe centers (Rosso et al. 1999). The S_2 dimer is located at the lower tunneling current sites (dark sites). The higher relative tunneling current at Fe sites at negative or positive bias voltage arises primarily from the dangling bond surface states which dominates the top of the valence band and forms the bottom of the conduction band at the surface. Upon exposure to O_2, the oxidative quenching of the surface states and the formation of Fe-O bonds should be reflected in the STM images as the transformation of bright unoxidized Fe sites to dark oxidized sites, as was seen on air oxidized pyrite by Eggleston et al. (1996).

Images collected on O_2 exposed samples show the development of distinct dark "patches" (Fig. 4) where surface Fe sites have been oxidized. Likewise, images collected simultaneously at both negative and positive bias (dual-mode STM) show the reduction of surface state density at both the valence and conduction band edges, localized on Fe (Fig. 5). Because imaging pyrite at the atomic scale proved to be a difficult task, "real-time" observations of oxidation progress were not feasible. However, observations of the atomic scale oxidation features, for both O_2 and O_2-H_2O dosed surfaces, showed a consistent set of characteristics. For the small range of tunneling conditions that led to the clearest atomic imaging, the tunneling current decrease from the average bright site to within a dark patch is the same within error as the difference between the bright Fe and the dark S_2 sites.

The patches are more often than not bounded by surface {11} or Fe-Fe directions, in agreement with oxidation in air (Eggleston et al. 1996). In the higher quality images of the oxidation patches, a decrease in tunneling current is observable at Fe sites bordering a patch (Figs. 5 and 6). This observation of atomic structure at the transition between oxidized and unoxidized domains is most readily apparent in the current images, rather than the topographic, or Z-piezo voltage images (e.g., Fig. 5). This may indicate that the oxidation of an Fe site may also draw state density from neighboring Fe sites, or there may be a decrease in the tunneling transmission probability due to an increase in the local workfunction at sites neighboring a patch. Workfunction increases are the general rule where sorbing species form a surface dipole with the negative end toward vacuum. This effect has been documented for the adsorption of Br_2 on in-vacuum cleaved pyrite (Pettenkofer et al. 1991), although no significant workfunction change was observed in this study using UPS. Therefore, the observation that decreased tunneling current sites border an oxidation patch probably equates to a strong local influence of oxidized Fe on
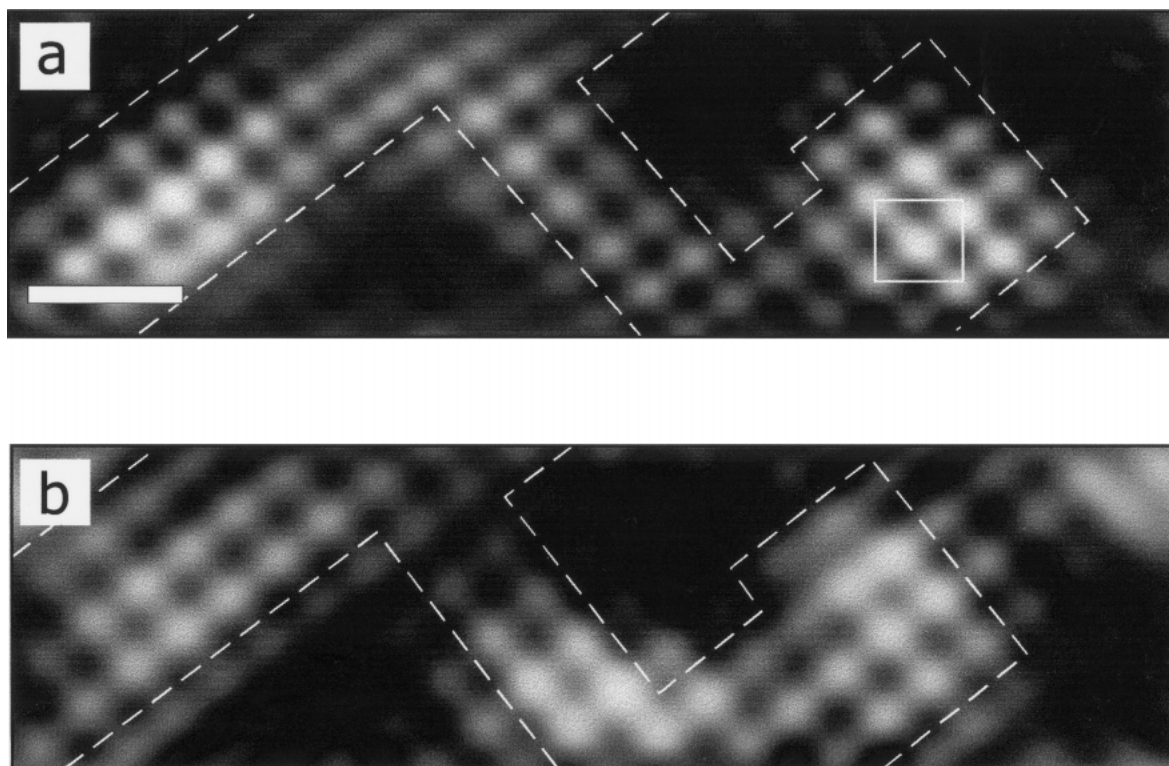

FIGURE 5. Dual-mode current UHV STM images collected simultaneously on pyrite {100} exposed to 4 L O_2. The tunneling conditions were –20 mV bias and 3 nA setpoint current (**a**), and 20 mV bias and 3 nA setpoint current (**b**). The scale bar represents 10 Å. The images were band pass FFT filtered to remove noise. Dark patches due to oxidation occur in both images indicating that state density is removed from both the valence and conduction band edges. A local reduction in the tunneling current at sites neighboring a patch can be generally seen as circumscribed by white dashed lines. Oxidation patches are generally bounded by <11> directions across the surface.
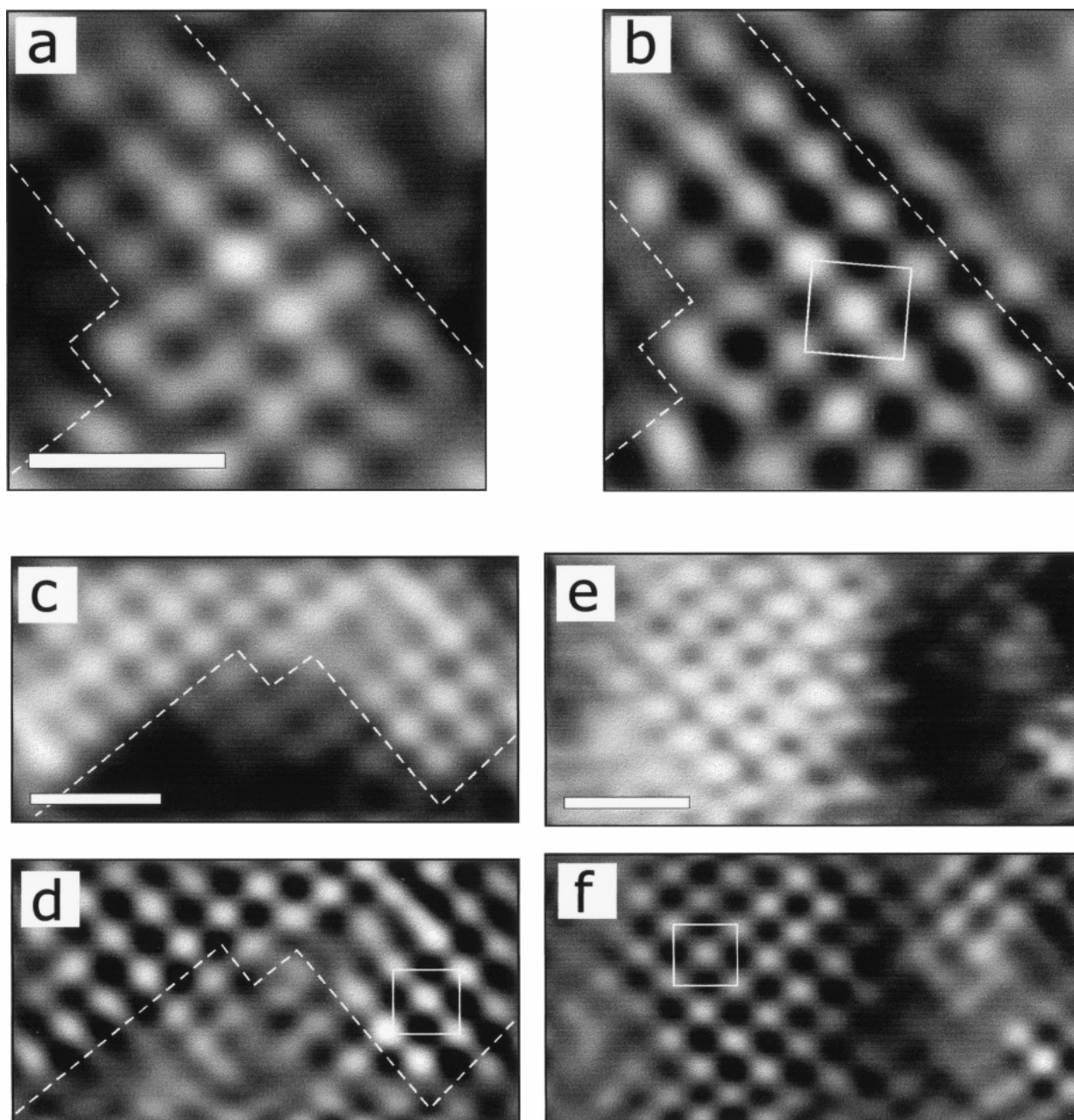
FIGURE 6. Topographic (**a,c**) and current (**b,d**) UHV STM images collected on pyrite {100} exposed to 4 L O_2. Topographic (**e**) and current (**f**) UHV STM images collected on pyrite {100} exposed to 0.4 L 40 mol% O_2 (O_2-H_2O). For all the images, the tunneling conditions were –0.1 V bias and 3 nA setpoint current, scale bar represents 10 Å, and all the images were band pass FFT filtered to remove noise. White dashed lines outline an oxidation patch. Unit cells are outlined by solid white squares.

the density of states of surrounding sites. This is similar to the effects predicted in calculated STM images of a PbS surface with sorbed O_2 (Becker and Hochella 1996).

In all the UHV STM images collected on O_2 exposed surfaces, unreacted areas on the surface were found, even for O_2 doses of up to 600 L, much greater than the point at which UPS indicated that the surface had "stopped" reacting (20 L). Thus, changes in the valence band structure between 0–20 L O_2, ob-

served by UPS, reflects the relatively rapid development of discrete oxidation patches. At higher doses, the surface oxidizes much more slowly, which is consistent with oxidation of the surface in air progressing slowly over a period of days using STM and UPS (Eggleston et al. 1996) and XPS (Nesbitt and Muir 1994). We suggest that the initial formation of oxidation patches involves surface sites of somewhat higher affinity for O_2, possibly surface defects.

The occurrence and reactivity of defects has been a focal point in recent studies of pyrite surfaces. The presence of linear defects at the atomic scale at an estimated occurrence of 0.05 defects per surface Fe site were demonstrated using STM in air (Eggleston et al. 1996). Although we observed no linear defects, a small proportion of point defects were found which we interpret as Fe vacancies attributed primarily to cleavage induced surface damage (Rosso et al. in preparation). The Fe 2p XPS tail-off intensity (Karthe et al. 1993) and the specific adsorption behavior of H_2O on UHV cleaned pyrite (Guevremont et al. 1997; Guevremont et al. 1998) has been attributed to S-deficient defect sites, which likewise have been projected to be present in the bulk crystal (Bronold et al. 1994) at 1% concentration (Birkholz et al. 1991). Because no direct evidence for a significantly high concentration of surface defects was found here, we can only tenuously ascribe the more reactive surface sites responsible for the birth of oxidation patches as similar to those described above.

From the UHV STM image data of surfaces exposed to low doses of O_2, the initial reactivity of the surface can be addressed, cast in terms of the sticking probability for O_2. The sticking probability is the fraction of the molecules that impinge on a surface and stick divided by the total number of impinging molecules. From the 4 L images (see Figs. 4–6), we estimate that, on average, 30% surface Fe sites have been oxidized. The exposure in Langmuirs (L) can be converted to that in molecules/cm² (Ex) by the relation (Masel 1996):

$$Ex = \frac{2.97 \cdot 10^{16}}{\sqrt{MT_g}} L$$

where M is the molecular weight of the gas (in AMU) and T_g is the gas temperature (in K). Using this equation, we calculate $\sim 1 \times 10^{15}$ molecules/cm² impinge on the surface for a 4 L exposure of O_2. Using Fe sites as the adsorption sites, then there are 6.8×10^{14} sites/cm² on a flat {100} terrace. Assuming for the moment that O_2 dissociatively sorbs (see ab-initio section below), then a sticking probability of 0.1 is calculated for O_2 impinging on a pristine UHV-cleaved {100} surface at room temperature.

Scanning tunneling spectroscopy

Tunneling spectroscopy involves measuring the dependence of the tunneling current on the bias voltage $I(V)$, which, when differentiated and normalized, can be nearly directly related to the sample density of states at the location of the tip. Local and area-averaged $I(V)$ tunneling spectra have been collected on these surfaces and have been successfully related to the surface DOS (Rosso et al. 1999). Averaged $I(V)$ tunneling spectra, showed a "flattening" in the shape of current response curve with O_2 exposure indicating an increasing insulating character to the surface (Fig. 7). Likewise, differential normalized tunneling spectra showed the progressive decrease in the DOS at the top of the valence band and the bottom of the conduction band (Fig. 8a), in agreement with the UPS observations. The loss of state density at the valence and conduction band edges is consistent with the consumption of the dangling bond states localized at Fe sites.
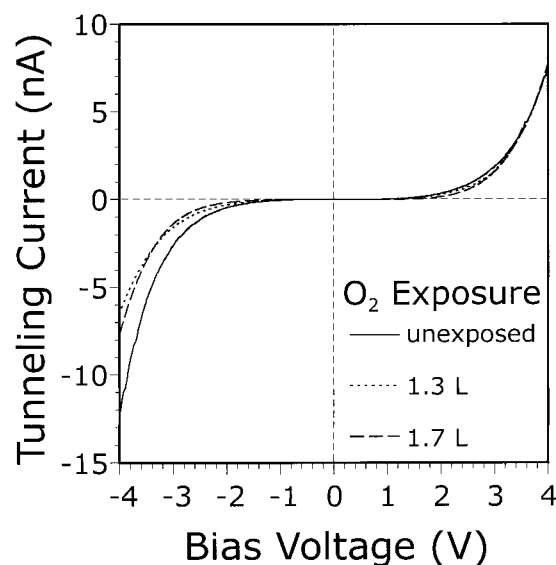

FIGURE 7. $I(V)$ area-averaged tunneling spectra collected over a random distribution of points on pristine and O_2 exposed surfaces. Each spectrum is the average of 125 spectra. The tunneling conditions were 4 V bias and 7 nA setpoint current.
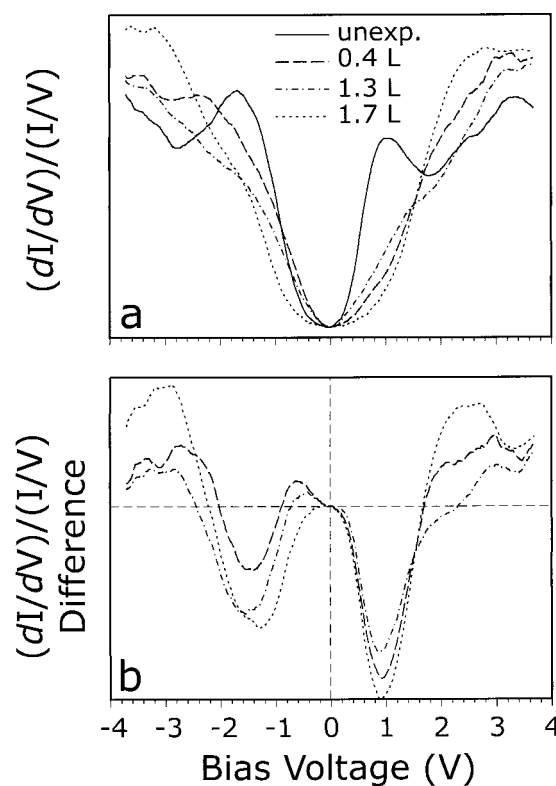

FIGURE 8. Area-averaged (dI/dV)/(I/V) tunneling spectra (**a**), and difference spectra (reacted-unreacted) (**b**) collected over a random distribution of points on pristine and O_2 exposed surfaces. Each spectrum for O_2 exposed surfaces is the average of 125 spectra. The tunneling conditions were 4 V bias and 7 nA setpoint current.

Difference tunneling spectra (Fig. 8b) show that the DOS decreases are focused at ~ –1.5 and +1 eV, and increases occur at –3 and 2.5 eV. Trends in the valence band changes, from the UPS (Fig. 1b) and STS data (Fig. 8b) are similar in that the loss of state density has a maximum in the vicinity of –1 eV. Likewise, this is followed by a more positive feature (–2 eV from UPS data, –3 eV from STS data) that is attributed to S 3p states. Some differences exist. The difference intensity of the S 3p feature is negative overall in the UPS data but positive in the STS spectra. This discrepancy is most likely due to the relative surface sensitivities of UPS compared with STS. The kinetic energy of the He I UPS photoelectrons from these S 3p states equates to an electron attenuation length of approximately 25 Å (Seah and Dench 1979). Therefore, the UPS data contain significant contributions from non-bonding Fe 3d states, which are progressively depopulated by sorbed O species causing a net loss in state density in the overlapping S 3p states. STS, on the other hand, is sensitive only to states that decay into the vacuum on the order of a few bond lengths (<10 Å) from the plane of the surface. Tunneling spectra of the in-vacuum cleaved surface show that contributions to state density in this range arise predominantly from dangling bond states and S 3p states (Rosso et al. 1999). The non-bonding Fe 3d states contribute only minor state density because, in the language of molecular orbital theory, the non-bonding d_{xz}, d_{yz}, and d_{xy} orbitals do not project normal to the plane of the surface. Thus, the S 3p feature in the difference STS spectra is less negative than that for the UPS data. An additional variable which may factor into the intensity discrepancy is related to the $(dI/dV)/(I/V)$ conversion, which becomes less accurate when the tunneling conductance begins to diverge from a perfectly exponential relationship (Hamers 1993). The $I(V)$ curves show a slight deviation from true exponential behavior, which could not be avoided (Fig. 7).

The discrepancies of the electron binding energy peak positions between the difference UPS and STS data can be related to a couple of factors. The first is due to difficulties in accurately unveiling the locations of the band edges in the conversion from $I(V)$ to $(dI/dV)/(I/V)$. The conversion mathematically diverges near the Fermi level for semiconductors because I approaches zero faster than V, causing a spike in the gap region. A simple but effective strategy for suppressing the spike is to add a small constant to the (I/V) denominator across the spectrum. This invariably has the effect of shifting the apparent energies of the band edges away from the Fermi level slightly.

Another factor is related to the effects of the varying electric field between the tip and the sample during the voltage ramp, usually referred to as tip-induced band bending. The high field between the tip and sample can significantly alter the positions of the bulk bands near the surface of wider band gap materials (Kaiser et al. 1988; Weimer et al. 1989). The effect spreads out the energies of the spectral features away from the Fermi level (Hamers 1993). In general, a high concentration of occupied dangling bond states on the surface of a semiconductor tends to fully screen the effects of this field on the band positions by changing the occupation of the surface states somewhat (Kaiser et al. 1988). Thus, in these experiments, the unexposed pyrite surface was most likely immune to the effects of tip induced band bending (Hamers 1993). However, as sorbed O species consume the dangling bond states, the screening potential of the surface states is reduced and the effects of tip-induced band bending may then become significant. The end result is an artificial displacement of the energy of the tunneling spectral features, like the valence band S 3p feature, away from the Fermi level.

Ab initio calculations

We modeled the {100} surface using gas phase calculations on an aperiodic cluster to reduce the computational costs and because of previous success with this strategy (e.g., Hermann and Bagus 1978; Siegbahn and Wahlgren 1991; Becker and Hochella 1996). The cluster used one fivefold-coordinated Fe site and two threefold-coordinated S sites on one surface (Fig. 9a) which are the respective bonding environments for the uppermost surface Fe and S sites on a flat terrace. Corner Fe sites (coordinated by 3 S atoms) were utilized as a basic model for surface "defect" sites consistent with the prevailing understanding that S-deficient defects can be present on the {100} surface to an appreciable degree (Birkholz et al. 1991; Karthe et al. 1993; Guevremont et al. 1997; Guevremont et al. 1998). Because the structure of these defects is not yet understood, the coordinatively undersaturated environment for a corner Fe site in the cluster can only be considered as a very simplistic analogy.

Oxygen. Geometry optimizations of the position of an O_2 molecule with respect to the cluster were performed spin unrestricted (spin multiplicity = 3) to accommodate the paramagnetic ground state of the free O_2 molecule. The O_2 molecule was found to preferentially "sorb" to the fivefold-coordinated surface Fe site by a total energy decrease of 9.2 kcal/mol (exothermic) (Fig. 9b). The stable adsorption geometry can be described as a tilted "end-on" configuration with the O closest to the Fe centered (Fe-O = 1.98 Å) along the Z axis of the C_{4v} bonding environment around the surface Fe, restoring the distorted octahedron as found around bulk Fe (Fig. 9b). Mulliken population and spin density analyses show that the O bonded to the Fe has a net charge of –0.49 and no unpaired spins, while the upper O is –0.13 and has 1 unpaired spin. The charge drawn to the O bonded to the Fe leads to spin pairing of one of the unpaired spins in the π^* orbital of the O_2 molecule, which also effectively lowers the O-O bond order from 2 to 1.5. This loss of bond strength is reflected in the longer O-O bond length for sorbed O_2 (1.38 Å) vs. that calculated for gaseous O_2 (1.21 Å). Likewise, the dissociation energy for sorbed O_2 is calculated to be 40% of that for free O_2, which suggests that O_2 is more prone to dissociate on the surface.

The sorbed O_2 molecule aligns itself between the largest separations of uppermost S sites, along Fe-Fe directions, owing to electrostatic repulsion between negatively charged O and S atoms (Fig. 9b). We tested the possibility that O_2 would dissociatively chemisorb by splitting the O_2 molecule into monoatomic O atoms over Fe sites along the Fe-Fe direction. Geometry optimizations of these O atoms suggest that this configuration (Fig. 9b) is strongly thermodynamically favored over sorbed molecular O_2, consistent with the predominant experimental observation of dissociative chemisorption for O_2 on a wide range of surfaces (see Zangwill 1988; Benzinger 1991; Henrich and Cox 1994). The large net energy lowering associ-
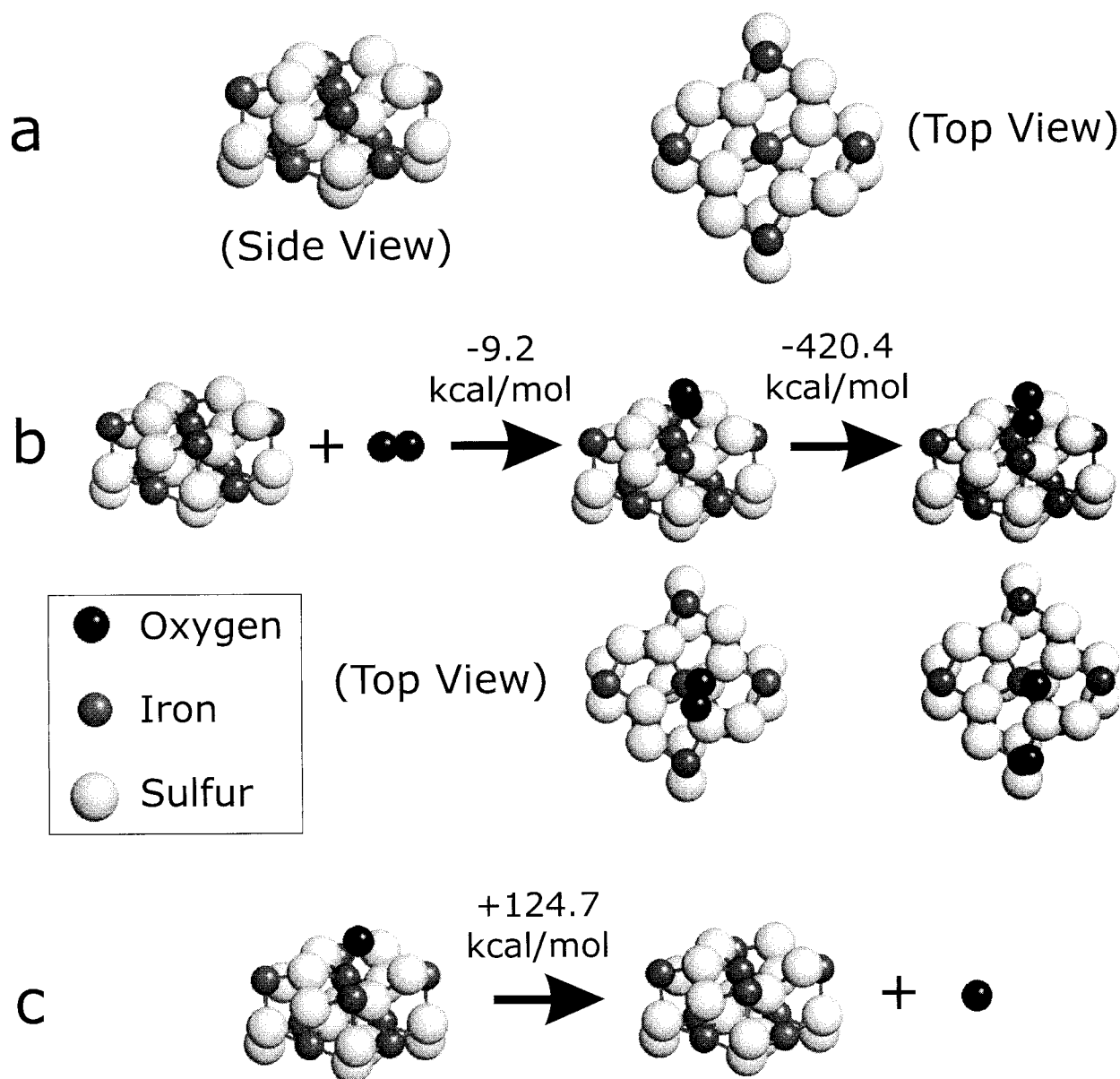
FIGURE 9. (a) 27-atom cluster of pyrite used for ab-initio calculations of the interaction of the {100} surface with O_2 and H_2O species. Also shown are optimized cluster configurations and reaction energies for the interaction of the pyrite {100} surface with O_2 (**b**) and O (**c**). A negative reaction energy means that the respective arrow points in the downhill direction. The calculations indicate that O_2 dissociatively chemisorbs to Fe sites.

ated with this configuration is obviously too large for typical adsorption processes due to the necessity of utilizing a undercoordinated corner Fe as an adsorption site for an O atom. However, based on the typical behavior of O_2 adsorption, we maintain that the dissociative adsorption process is substantially downhill. To more accurately investigate the properties of sorbed O at a typical terrace Fe site, we utilized clusters shown in Figure 9c. Monoatomic O_2 sorbs in an "on-top" configuration over the center Fe site, with a Fe-O bond length of 1.96 Å and a bond energy of 124.7 kcal/mol. The sorbed O draws charge from the cluster and is best characterized as chemi-

sorbed O^- (Mulliken charge = –0.61) having one unpaired spin. The Mulliken charge on the surface Fe of the Fe-O bond becomes slightly more positive but not enough to suggest that its formal charge should be considered Fe^{3+}. Taken altogether, the calculation results for the adsorption behavior of O_2 are consistent with our experimental observations and those of Pettenkofer et al. (1991) for the sorption behavior of the oxidant Br_2 on pyrite {100}.

Water. Geometry optimizations of H_2O and related species are shown in Figure 10. The calculations indicate that the sorption of molecular H_2O at surface Fe sites is thermodynamically

favorable, but with much less driving force than that for the dissociative chemisorption of O_2. The H_2O molecule sorbs with the negative end of its dipole toward the surface, in agreement with the experimental observations at 100 K (Pettenkofer et al. 1991). The sorbed H_2O molecule is best characterized as physisorbed since the sum of the Mulliken charges for the H_2O molecule is 0.03, indicating no charge transfer. The adsorption energies for molecular H_2O over the center (Fig. 10a) and a corner (Fig. 10b) Fe site are estimated to be exothermic by 50.8 and 57.8 kcal/mol respectively. In a recent study by Guevremont et al. (1998), the desorption energy difference for molecular H_2O from surface Fe sites and S-deficient defect sites was measured to be 5 kcal/mol using temperature programmed desorption. Thus, although these calculations incorrectly predict that H_2O should molecularly sorb to the pyrite surface at room temperature, the direct comparison of cluster energies gives values consistent with experiment, assuming the corner Fe site is representative of a S-deficient surface defect. Comparison of the energies of the molecularly sorbed H_2O cases with various optimized configurations of dissociated H_2O spe-

cies (Fig. 10c–f) indicate that the dissociation of H_2O on the surface is not thermodynamically favored, in agreement with experiment (Pettenkofer et al. 1991; Guevremont et al. 1998).

Oxygen and Water. Various configurations of H_2O, H_2O-derived species, and O^- were optimized for geometry on the upper surface of the cluster (Fig. 11). Because the dissociative chemisorption of O_2 is strongly downhill, monoatomic O was optimized over the center Fe site along with OH^- and H^+ at either corner Fe sites or surface S sites. The co-adsorption of molecular H_2O and O^- at Fe sites is calculated to be thermodynamically downhill by 42.5 kcal/mol (Fig. 11a). However, the adsorption energy is lower than for the individual H_2O and O^- adsorption cases, which may suggest that co-adsorption reactions for surfaces exposed to O_2-H_2O mixtures is an activated process. The most thermodynamically favorable configuration occurs when O^- and dissociated H_2O species are sorbed to Fe sites (Fig. 11b). The geometry optimized configuration in Figure 11b is favored by 23.6 kcal/mol over that in Figure 11a. The O^- is more strongly sorbed to the center Fe for the dissociated H_2O case (1.96 Å, Fig. 11c) than for the molecular H_2O
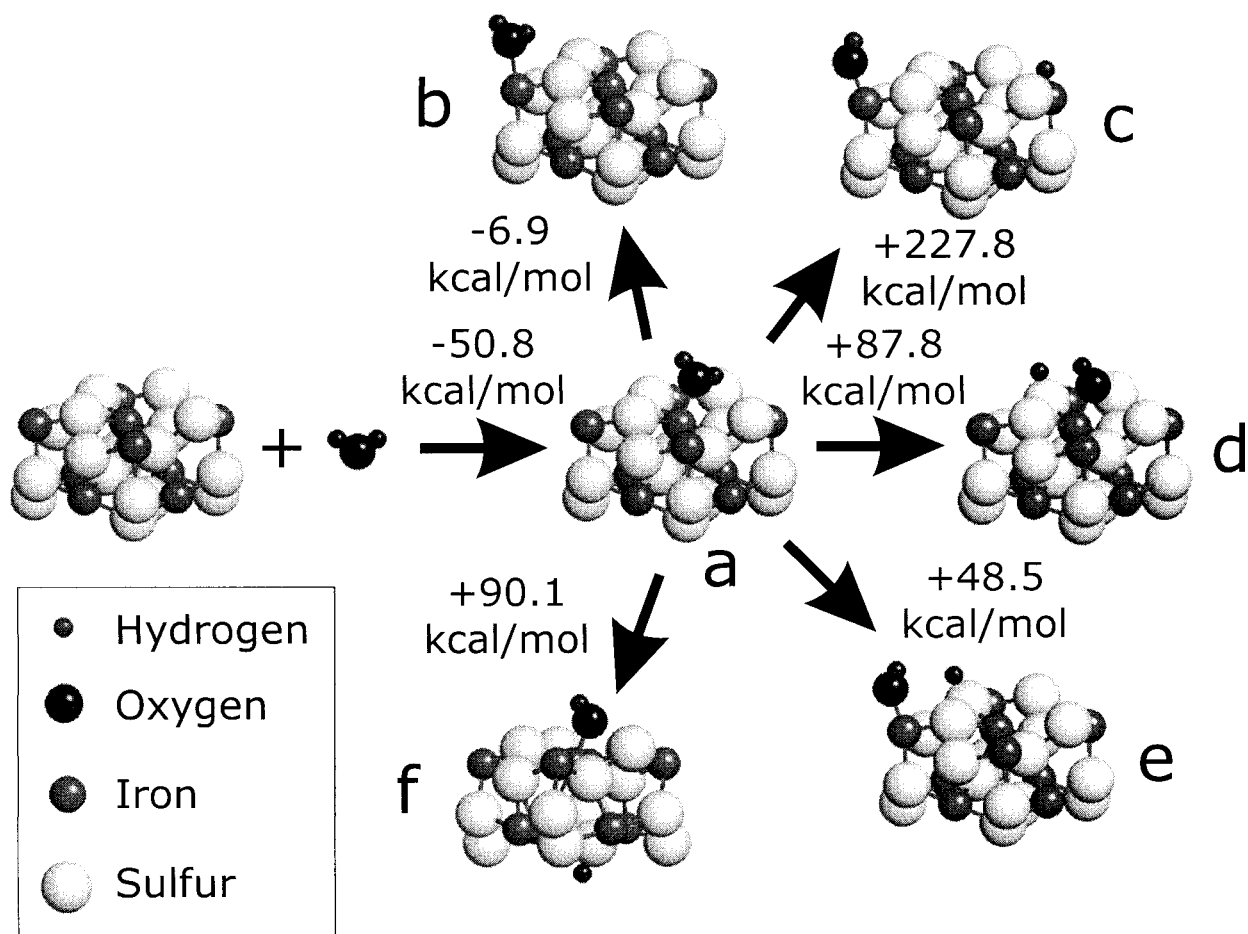

FIGURE 10. Optimized cluster configurations and reaction energies for the interaction of the pyrite {100} surface with H_2O (**a**, **b**) and dissociated H_2O (**c– f**) species. A negative reaction energy means that the respective arrow points in the downhill direction. The calculations indicate that H_2O molecularly physisorbs to Fe sites.

case (2.02 Å, Fig. 11b). Likewise, the O-H bond lengths for the case shown in Figure 11b are 0.96 Å and 0.94 Å, which, when compared with the O-H distance in free H_2O (0.95 Å), indicates a slight strengthening of one O-H bond and a slight weakening of the other. Collectively, these observations mean that although the dissociation of H_2O on the H_2O-exposed surface is energetically uphill (>48.5 kcal/mol), it is downhill on the O_2/H_2O exposed surface. This can be understood based on simple charge budget arguments. In the configuration in Figure 11b, electrons drawn from the cluster Fe and S atoms into the sorbed O^- are replenished by surface hydroxyls. The balancing of charge transfers to and from surface sites with the combination of sorbed O and H_2O-derived species is the most energetically favorable method to quench Fe dangling bonds.

In the adsorbed O^- calculations (Fig. 9), Mulliken population analyses of the upper surface atoms show that the electronic charge that is drawn from the cluster to populate the sorbed O^- atom depletes the Fe and the two threefold-coordinated S sites. The formation of Fe-O bonds at the expense of negative charge at S sites may increase the susceptibility of

surface S sites to hydrophyllic attack. Such a mechanism would be consistent with the experimental observations of Taylor et al. (1984) and Reedy et al. (1991) that O_2 in the end-product sulfate is primarily derived from dissociated H_2O. This question was tested by geometry optimizing the coordinates of an OH^- over a surface S site, with and without the presence of sorbed O^- at the center Fe site. In the case without any sorbed O present on the cluster, the OH^- does not sorb to surface S. However, with O^- sorbed, OH^- sorbed to a surface S site is a stable configuration (Fig. 11d), partly stabilized by the charge depletion due to sorbed O^- and partly due to hydrogen bonding to the sorbed O^- (OH-O = 1.71 Å). Yet, this configuration is thermodynamically unfavorable. The sorbed OH^- is trapped in a local minimum, the global minimum for which is the case shown in Figure 11b. These calculations demonstrate that the proposed hydrolysis of surface S is chemically plausible in the presence of sorbed O^-, but the question of whether or not this mechanism becomes dominant at more advanced stages of surface oxidation is difficult to address at this stage due to the required increase in computational costs.
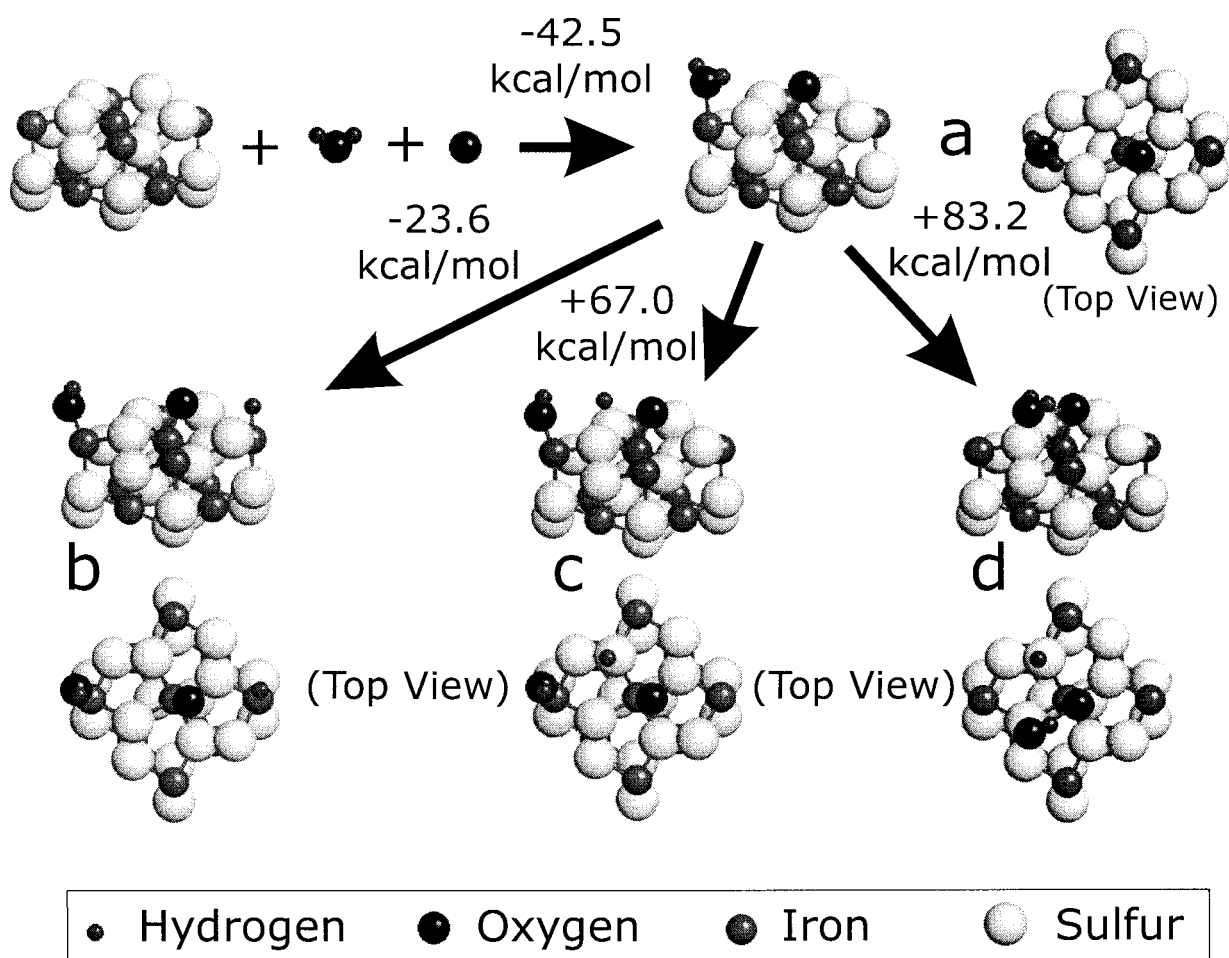

FIGURE 11. Optimized cluster configurations and reaction energies for the interaction of the pyrite {100} surface with O_2 and H_2O species. A negative reaction energy means that the respective arrow points in the downhill direction. The calculations indicate that the co-adsorption of H_2O and O_2 (O–) on surface Fe sites is energetically downhill (a). Sorbed H_2O preferentially dissociates on the surface when co-adsorbed with O_2 (b).

IMPLICATIONS

The high density of Fe 3d dangling bonds across the {100} surface dictates the sorption behavior of both O_2 and H_2O. The formation of Fe-O⁻ and Fe-OH⁻ bonds across the surface are precursors to the formation of Fe(III) oxides and oxyhydroxides, which have been experimentally observed using XPS to form on air oxidized pyrite before the formation of S oxidation products such as sulfate using XPS (Nesbitt and Muir 1994). Atomic-scale images of oxidation features show a local influence of oxidized Fe sites on the density of states of neighboring Fe sites. This effect is generally limited to nearest and next nearest neighbors adjacent to an oxidation patch. Its effect on the overall reactivity of the surface is difficult to quantify. Eggleston et al. (1996) modeled surface oxidation patches as discrete semi-conducting phases with state density within the bulk band gap of pyrite. Our STM-STS data demonstrates that, at least for the initial stages of oxidation, surface state density decreases with oxidation progress. However, the adsorption and electron transfer reactions investigated here pertain only to the development of incipient product phases, whereas in the study by Eggleston et al. (1996), oxidation progress was possibly more advanced.

The theoretical prediction of preferential interaction of O_2 and H_2O derived species with Fe 3d states, and not S 3p states, is in agreement with the appearance of a more positive S 3p DOS feature just below the valence band edge, as indicated by UPS and STS difference spectra. Population analyses of O⁻ sorbed cluster calculations show that surface S sites are partially depopulated by the formation of Fe-O bonds and thereby the S sites become slightly more electropositive. This increases the susceptibility of surface S site to hydrophyllic attack and may eventually lead to the production of S-O bonds on the surface, as precursors to sulfate, consistent with the observation that oxygen, in the end product sulfate, is largely derived from H_2O.

This behavior is consistent with an electrochemical oxidation mechanism where electron transfers to and from the surface take place at distinct anodic and cathodic sites. Perhaps the most salient outcome of this investigation is the evidence that such a mechanism can occur. Both the experiments and modeling calculations point to the importance of the roles of O_2 and H_2O as combined reactants for the most effective adsorption to the surface, with Fe sites mediating as both anodic and cathodic sites. The cathodic reaction is the dissociative chemisorption of O_2, and the anodic reaction is the dissociation of molecularly sorbed H_2O. The coupled reactions provide a possible mechanism for the production of dissociated H_2O species at the pyrite surface, a necessary precursor to the development of sulfate.

ACKNOWLEDGMENTS

REFERENCES CITED

Becker, U., and Hochella, M.F. Jr. (1996) The calculation of STM images, STS spectra, and XPS peak shifts for galena: New tools for understanding mineral surface chemistry. Geochimica et Cosmochimica Acta, 60, 2413–2426.

Benzinger, J.B. (1991) Thermochemical methods for reaction energetics on metal surfaces. In E. Shustorovich, Ed., Metal-surface reaction energetics, p. 53–107. VCH, New York.

Birkholz, M., Fiechter, S., Hartmann, A., and Tributsch, H. (1991) Sulfur deficiency in iron pyrite (FeS_{2-x}) and its consequences for band-structure models. Physical Review B, 43, 11926–11936.

Bronold, M., Pettenkofer, C., and Jaegermann, W. (1994) Surface photovoltage measurements on pyrite (100) cleavage planes: Evidence for electronic bulk defects. Journal of Applied Physics, 76, 5800–5808.

Brundle, C.R. (1974) The application of electron spectroscopy to surface studies. Journal of Vacuum Science and Technology, 11, 212–224.

Buckley, A.N. and Woods, R. (1987) The surface oxidation of pyrite. Applied Surface Science, 27, 437–452.

Dunning, T.H. and Hay, P.J. (1976) In H.F. Schaefer, III, Ed., Modern Theoretical Chemistry, p. 1–28. Plenum, New York.

Eggleston, C.M. (1994) High resolution scanning probe microscopy: Tip-surface interaction, artifacts, and applications in mineralogy and geochemistry. In Clay Minerals Society Workshop Lectures, 7, 1–90.

Eggleston, C.M., Ehrhardt, J.-J., and Stumm, W. (1996) Surface structural controls on pyrite oxidation kinetics: An XPS-UPS, STM, and modeling study. American Mineralogist, 81, 1036–1056.

Frisch, M.J. et al. (1995) Gaussian 94 (Revision C.2) Gaussian, Inc., Pittsburgh PA.

Goldhaber, M.B. (1983) Experimental study of metastable sulfur oxyanion formation during pyrite oxidation at pH 6–9 and 30 °C. American Journal of Science, 283, 193–217.

Guevremont, J.M., Strongin, D.R., and Schoonen, M.A.A. (1997) Effects of surface imperfections on the binding of CH_3OH and H_2O on FeS_2 (100): Using adsorbed Xe as a probe of mineral surface structure. Surface Science, 391, 109–124.

Guevremont, J.M., Strongin, D.R., and Schoonen, M.A.A. (1998) Photoemission of adsorbed Xenon, X-ray photoelectron spectroscopy, and temperature-programmed desorption studies of H_2O on FeS_2 (100). Langmuir, 14, 1361–1366.

Hamers, R.J. (1993) Methods of tunneling spectroscopy with the STM. In D.A. Bonnell, Ed., Scanning tunneling microscopy and spectroscopy: Theory, techniques, and applications, p. 51–103. VCH, New York.

Henrich, V.E. and Cox, P.A. (1994) The surface science of metal oxides, 464 p. Cambridge University Press, U.K.

Hermann, K. and Bagus, P.S. (1978) Cluster studies of the interaction of oxygen with the lithium (100) surface. Physical Review B, 17, 4082–4099.

Kaiser, W.J., Bell, L.D., Hecht, M.H., and Grunthaner, F.J. (1988) Scanning tunneling microscopy characterization of the geometric and electronic structure of hydrogen-terminated silicon surfaces. Journal of Vacuum Science and Technology A, 6, 519–523.

Karthe, S., Szargan, R., and Suoninen, E. (1993) Oxidation of pyrite surfaces: A photoelectron spectroscopic study. Applied Surface Science, 72, 157–170.

Kurtz, R.L., Stockbauer, R., Madey, T.E., Román, E., and de Segovia, J.L. (1989) Synchrotron radiation studies of H_2O adsorption on TiO_2 (110). Surface Science, 218, 178–200.

Li, E.K., Johnson, K.H., Eastman, D.E., and Freeouf, J.L. (1974) Localized and bandlike valence electron states in FeS_2 and NiS_2. Physical Review Letters, 32, 470–472.

Masel, R.I. (1996) Principles of adsorption and reaction on solid surfaces, 804 p., Wiley, New York.

McKibben, M.A. and Barnes, H.L. (1986) Oxidation of pyrite in low temperature acidic solutions: Rate laws and surface textures. Geochimica et Cosmochimica Acta, 50, 1509–1520.

Moses, C.O. and Herman, J.S. (1991) Pyrite oxidation at circumneutral pH. Geochimica et Cosmochimica Acta, 55, 471–482.

Moses, C.O., Nordstrom, D.K., Herman, J.S., and Mills, A.L. (1987) Aqueous pyrite oxidation by dissolved O_2 and by ferric iron. Geochimica et Cosmochimica Acta, 51, 1561–1571.

Mycroft, J.R., Bancroft, G.M., McIntyre, N.S., Lorimer, J.W., and Hill, I.R. (1990) Detection of sulphur and polysulphides on electrochemically oxidized pyrite surfaces by X-ray photoelectron spectroscopy and Raman spectroscopy. Journal of Electroanalytical Chemistry, 292, 139–152.

Nesbitt, H.W. and Muir, I.J. (1994) X-ray photoelectron spectroscopic study of a pristine pyrite surface reacted with H_2O vapor and air. Geochimica et Cosmochimica Acta, 58, 4667–4679.

Nicholson, R.V., Gillham, R.W., and Reardon, E.J. (1988) Pyrite oxidation in carbonate-buffered solution: I. Experimental kinetics. Geochimica et Cosmochimica Acta, 52, 1077–1085.

Pettenkofer, C., Jaegermann, W., and Bronold, M. (1991) Site specific surface interaction of electron donors and acceptors on FeS_2 (100) cleavage planes. Berichte der Bunsen-Gesellschaft fur Physikalische Chemie, 95, 560–565.

Reedy, B.J., Beattie, J.K., and Lowson, R.T. (1991) A vibrational spectroscopic ¹⁸O tracer study of pyrite oxidation. Geochimica et Cosmochimica Acta, 55, 1609–1614.

Rosso, K.M, Becker U., and Hochella, M.F. Jr. (1999) Atomically resolved electronic structure of pyrite {100} surfaces: An experimental and theoretical investigation with implications for reactivity. American Mineralogist, 84, 1535–1548.

Schaufuss, A.G., Nesbitt, H.W., Kartio, I., Laajalehto, K., Bancroft, G.M., Szargan, R. (1998) Reactivity of surface chemical states on fractured pyrite. Surface Science, 411, 321–328.

Seah, M.P. and Dench, W.A., (1979) Quantitative electron spectroscopy of surfaces: A standard data base for electron mean free paths in solids. Surface and Interfacial Analysis, 1, 2–11.

Siegbahn, P.E.M. and Wahlgren, U. (1991) Cluster modeling of chemisorption energetics. In E. Shustorovich, Ed., Metal-surface reaction energetics, p. 1–52. VCH, New York.

Stevens, W.J., Basch, H., and Krauss, M. (1984) Compact effective potentials and efficient shared-exponent basis sets for the first- and second-row atoms. Journal of Chemical Physics, 81, 6026.

Stevens, W.J., Krauss, M., Basch, H., Jasien, P.G. (1992) Relativistic compact effective potentials and efficient, shared-exponent basis-sets for the 3rd-row, 4th-row, and 5th-row atoms. Canadian Journal of Chemistry, 70, 612–630.

Taylor, B.E., Wheeler, M.C., and Norstrom, D.K. (1984) Stable isotope geochemistry of acid mine drainage: Exerimental oxidation of pyrite. Geochimica et Cosmochimica Acta, 48, 2669–2678.

Van der Heide, H., Hemmel, R., van Bruggen, C.F., and Haas, C. (1980) X-ray photoelectron spectra of 3d transition metal pyrites. Journal of Solid State Chemistry, 33, 17–25.

Wagner, L.F. and Spicer, W.E. (1974) Photoemission study of the effect of bulk doping and O_2 exposure on silicon surface states. Physical Review B, 9, 1512–1515.

Weimer, M., Kramar, J., and Baldeschwieler, J. (1989) Band bending and the apparent barrier height in scanning tunneling microscopy. Physical Review B, 39, 5572–5575.

Wiersma, C.L. and Rimstidt, J.D. (1984) Rates of reaction of pyrite and marcasite with ferric iron at pH 2. Geochimica et Cosmochimica Acta, 48(1), 85–92.

Williamson, M.A. and Rimstidt, J.D. (1994) The kinetics and electrochemical rate-determining step of aqueous pyrite oxidation. Geochimica et Cosmochimica Acta, 58, 5443–5454.

Zangwill, A. (1988) Physics at surfaces, 454 p. Cambridge University Press, U.K